

**Low-temperature magnetic properties of NpNi<sub>5</sub>**A. Hen,<sup>1,2</sup> E. Colineau,<sup>1</sup> R. Eloirdi,<sup>1</sup> J.-C. Griveau,<sup>1</sup> N. Magnani,<sup>1</sup> F. Wilhelm,<sup>3</sup> A. Rogalev,<sup>3</sup> J.-P. Sanchez,<sup>4,5</sup> A. B. Shick,<sup>6</sup> I. Halevy,<sup>7,2</sup> I. Orion,<sup>2</sup> and R. Caciuffo<sup>1</sup><sup>1</sup>*European Commission, Joint Research Centre (JRC), Institute for Transuranium Elements (ITU), Postfach 2340, D-76125 Karlsruhe, Germany*<sup>2</sup>*Nuclear Engineering Department, Ben Gurion University, Beer-Sheva, Israel*<sup>3</sup>*European Synchrotron Radiation Facility (ESRF), B.P.220, F-38043 Grenoble, France*<sup>4</sup>*CEA, INAC-SPSMS, FR-38000 Grenoble, France*<sup>5</sup>*Université de Grenoble Alpes, INAC-SPSMS, FR-38000 Grenoble, France*<sup>6</sup>*Institute of Physics, ASCR, Na Slovance 2, CZ-18221 Prague, Czech Republic*<sup>7</sup>*Physics Department, Nuclear Research Center Negev, P.O. Box 9001, Beer-Sheva, Israel*

(Received 15 July 2014; revised manuscript received 24 July 2014; published 11 August 2014)

We present the result of an extended experimental characterization of the hexagonal intermetallic Haucke compound NpNi<sub>5</sub>. By combining macroscopic and shell-specific techniques, we determine the  $5f$ -shell occupation number  $n_f$  close to 4 for the Np ions, together with orbital and spin components of the ordered moment in the ferromagnetic phase below  $T_C = 16$  K ( $\mu_S = -1.88 \mu_B$  and  $\mu_L = 3.91 \mu_B$ ). The apparent coexistence of ordered and disordered phases observed in the Mössbauer spectra is explained in terms of slow relaxation between the components of a quasitriplet ground state. The ratio between the expectation value of the magnetic dipole operator and the spin magnetic moment ( $3\langle T_z \rangle / \langle S_z \rangle = +1.43$ ) is positive and large, suggesting a localized character of the  $5f$  electrons. The angular part of the spin-orbit coupling ( $\langle \vec{l} \cdot \vec{s} \rangle = -5.55$ ) is close to the value of  $-6.25$  calculated for trivalent Np ions in intermediate coupling approximation. The results are discussed against the prediction of first-principle electronic structure calculations based on the spin-polarized local spin density approximation plus Hubbard interaction, and of a mean field model taking into account crystal field and exchange interactions.

DOI: [10.1103/PhysRevB.90.054408](https://doi.org/10.1103/PhysRevB.90.054408)

PACS number(s): 75.10.Dg, 76.80.+y, 78.70.Dm, 71.15.Mb

**I. INTRODUCTION**

The Haucke intermetallic compound NpNi<sub>5</sub> was discovered during systematic investigations of the neptunium-nickel phase diagram motivated by the search of optimal targets for minor actinides transmutation processes, and by concerns related to the safety of nuclear fuels interacting with cladding materials [1]. X-ray diffraction showed that NpNi<sub>5</sub> (contrary to the cubic UNi<sub>5</sub>) has a hexagonal crystal symmetry and shares the CaCu<sub>5</sub> structure type with the Th and Pu analogs. Based on the lattice parameters, the authors of Ref. [1] derived a metallic radius of 0.1750 nm for the Np atoms in NpNi<sub>5</sub>. According to Zachariasen [2], such a value would correspond to a Np<sup>4+</sup> ( $5f^3$ ) oxidation state. Moreover, as the interatomic spacing of about 0.4 nm between Np atoms is substantially larger than the Hill limit (0.325 nm), the  $5f$  electrons should be localized [3] and appreciable crystal field effects are expected.

More information on the physical properties of NpNi<sub>5</sub> is not available. On the other hand, the literature on the isostructural RNi<sub>5</sub> compounds ( $R =$  rare earth) is much wider. Several members of this system react reversibly with hydrogen and can absorb it in large quantities at ambient temperatures and pressures [4–8]. They have therefore been widely investigated for their potential as hydrogen and electrochemical storage material. Also the magnetic properties of RNi<sub>5</sub> compounds have attracted considerable attention, mainly because of their magnetocrystalline anisotropy, related to the interplay of crystal field (CF), spin-orbit, and exchange interactions acting on the  $R^{3+}$  ions [9–15]. In fact, as the  $3d$  band of Ni is almost filled by the rare earth valence electrons [16], the magnetic

properties of RNi<sub>5</sub> are almost entirely due to the  $R$  ions. For nonmagnetic rare earth ( $R =$  La, Ce, Lu, and Y), the compounds are enhanced Pauli paramagnets, otherwise they are ferromagnetic, with the highest  $T_C = 32$  K exhibited by GdNi<sub>5</sub> [16,17]. An exception is PrNi<sub>5</sub>, which is characterized by a well-isolated singlet CF ground state, and is therefore a Van Vleck paramagnet [18–21].

Here, we present the results obtained by superconducting quantum interference device (SQUID) magnetometry, specific heat, Mössbauer spectroscopy, and x-ray magnetic circular dichroism (XMCD) measurements carried out on NpNi<sub>5</sub> polycrystalline samples. We show that the compound orders ferromagnetically below  $T_C = 16$  K, with an ordered moment  $\mu_{Np} \sim 2 \mu_B$  carried out by Np<sup>3+</sup> ions and a very small contribution ( $\sim 0.08 \mu_B$  per Ni atom) from the Ni sublattice. Information on the low-energy part of the electronic spectrum is obtained from the analysis of the specific heat curve. A combined analysis of the different experimental data sets allowed us to determine key parameters associated with the electronic structure of the system. These results are used to benchmark the predictions of first principle electronic structure calculation based on the spin-polarized local spin density approximation plus Hubbard interaction.

The remainder of this paper is structured as follows. In Sec. II, we provide details on synthesis and experimental procedures; in Sec. III we present the experimental results and compare them with the outcome of mean-field calculations. The results of first principle calculations are presented in Sec. IV. Discussion and conclusions are found in Secs. V and VI.

## II. EXPERIMENTAL DETAILS

Polycrystalline samples of  $\text{NpNi}_5$  were prepared by arc melting stoichiometric amounts of high-purity elemental constituents (99.9% Np, 99.999% Ni) on a water-cooled copper hearth, under Ar (6N) atmosphere. A Zr alloy was used as an oxygen getter. The weight losses were examined after arc melting and found to be less than 0.5%. The sample was melted five times and crushed before the last melt, to ensure complete homogeneity of the alloy button. The same procedure has been followed to prepare a sample of the nonmagnetic isostructural compound  $\text{ThNi}_5$ , which has been used to determine the vibrational contribution to the specific heat of  $\text{NpNi}_5$ .

Crystallographic phase analyses were performed at room temperature by x-ray diffraction on samples with a mass of about 25 mg, finely ground and dispersed on a Si wafer. Data were collected in reflection mode with a Bruker D8 diffractometer installed inside a  $\alpha - \gamma$  glove box, using  $\text{Cu-K}\alpha_1$  radiation ( $\lambda = 0.15406$  nm) selected by a Ge (111) monochromator. A 1-D position sensitive detector was used to cover the angular range from 15 to 120 degrees, with incremental steps of 0.0085 degrees.

dc-magnetization and magnetic susceptibility measurements were carried out in the temperature range 2–300 K, with an external magnetic field up to 7 T on a 196 mg sample using the MPMS-7 SQUID from Quantum Design (QD). The specific heat experiments were performed using the relaxation method on a 10.9 mg polycrystalline sample using the QD PPMS-14 platform in the temperature range 2.2–300 K and in a magnetic field up to 14 T. For these measurements, the sample was enrobed in Stycast<sup>®</sup> 1266 epoxy encapsulant, to prevent external radioactive contamination. The resin contribution to the measured heat capacity was subtracted according to a standard procedure. The  $^{237}\text{Np}$  Mössbauer measurements were performed in transmission geometry on a powder absorber with a thickness of  $140 \text{ mg cm}^{-2}$  of Np. The Mössbauer source ( $\sim 108 \text{ mCi}$  of  $^{241}\text{Am}$  metal) was kept at 4.2 K, while the temperature of the absorber was varied from 4.2 to 140 K in discreet steps. The spectra were recorded with a sinusoidal drive system using conventional methods. The velocity scale was calibrated with reference to a  $\text{NpAl}_2$  standard ( $B_{hf} = 330 \text{ T}$  at 4.2 K). No contributions associated with the small amount of  $\text{NpO}_2$  impurity phase have been observed in the measured quantities. In particular no anomaly was visible around 25 K, the temperature below which long-range order of magnetic triakontadipoles is stabilized in  $\text{NpO}_2$  [22,23].

The x-ray-absorption-spectroscopy (XAS) and x-ray magnetic circular dichroism (XMCD) experiments were carried out at the European Synchrotron Radiation Facility (ESRF) using the ID12 beamline, which is dedicated to polarization-dependent spectroscopy in the photon-energy range from 2 to 15 keV. Data were collected at the  $M_{4,5}$  edges of Np (3.6–3.9 keV). After monochromatization with a double-crystal Si(111), the rate of circular polarization of the photons provided by the Helios-II helical undulator (in excess of 0.95) was reduced to about 0.42 at the  $M_5$  and 0.50 at the  $M_4$  absorption edge. The x-ray-absorption spectra were recorded using the total-fluorescence-yield detection mode in backscattering geometry for parallel  $\mu^+(\text{E})$  and antiparallel  $\mu^-(\text{E})$  alignments of the photon helicity with respect to a

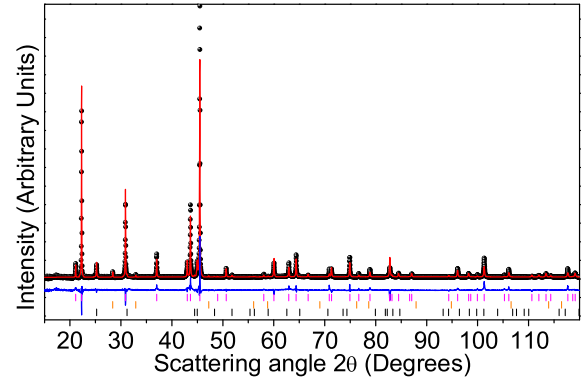


FIG. 1. (Color online) Observed (dots) and calculated (red line) x-ray diffraction pattern recorded at room temperature for  $\text{NpNi}_5$ . The lower trace (blue line) is the difference profile. The intensity distribution is plotted as a function of the full diffraction angle  $2\theta$  ( $\text{Cu K}\alpha_1$  radiation). Vertical ticks indicate calculated angular positions of the Bragg peaks for (upper row, magenta) the  $\text{NpNi}_5$  phase, (middle row, orange) an impurity phase ( $\text{NpO}_2$ ,  $\sim 3\%$  in weight), and (lower row, black) a  $\text{SiO}_2$  contamination from the quartz mortar.

7 T external magnetic field applied along the beam direction. In order to get XMCD spectra free of experimental artifacts, measurements were also performed for the opposite direction of the applied magnetic field. For these measurements, we used a 3.5 mg sample glued with a conductive resin (Dupont 4929) inside an Al capsule, with a  $100\text{-}\mu\text{m}$ -thick Be window and a  $13\text{-}\mu\text{m}$ -thick kapton foil for protection.

## III. EXPERIMENTAL RESULTS

### A. Crystal structure

The room temperature powder diffraction pattern of  $\text{NpNi}_5$  is shown in Fig. 1. The Rietveld analysis was performed with the X'Pert HighScore Plus software package of PANalytical. The background was fitted with a sixth-order polynomial, and the shape of the Bragg peaks was described by a pseudo-Voigt function. The observed Bragg peaks can be indexed in the hexagonal  $P6/mmm$  space group, with lattice parameters  $a = 0.48501(5)$  nm and  $c = 0.39841(2)$  nm, in very good agreement with previous estimates [1]. Additional observed Bragg peaks reveal the presence of  $\text{NpO}_2$  as an impurity phase ( $\sim 3\%$  in weight) and some  $\text{SiO}_2$  from the agate mortar used to grind the sample. No other impurities were observed.

The best fit was obtained assuming the  $\text{CaCu}_5$ -type structure typical of Haucke compounds, with full occupation of  $1a$ ,  $2c$ , and  $3g$  sites and fixed isotropic temperature factors  $B$  ( $B_{\text{Np}} = 0.2 \text{ \AA}^2$ ;  $B_{\text{Ni}} = 0.4 \text{ \AA}^2$ ). Any attempt to vary the occupancy of additional sites resulted in an increase of the weighted-pattern index ( $R_{\text{wp}} = 0.13$ ). The crystal structure is shown in Fig. 2. The  $z = 0$  plane contains Np and Ni atoms located, respectively, at the  $1a$  and  $2c$  special positions, while the plane at  $z = 1/2$  contains Ni atoms centered at the  $3g$  Wyckoff sites. The first, second, and third neighbors of Np are 6 Ni ( $2c$ ), 12 Ni ( $3g$ ), and 2 Np, respectively. The smallest nearest Np-Np distance is of  $0.39841(5)$  nm, well above the so-called Hill limit of  $\sim 0.32$  nm that separates Np compounds

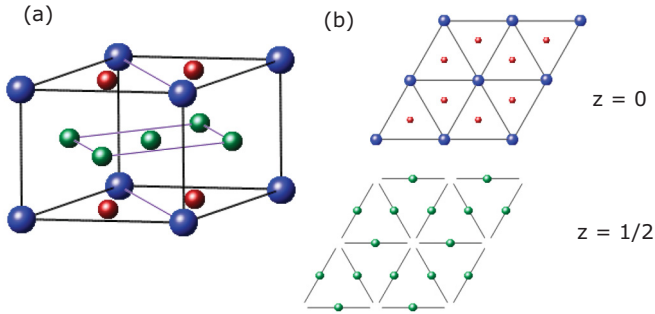


FIG. 2. (Color online) (a) Crystallographic unit cell of the Haucke hexagonal intermetallic compound NpNi<sub>5</sub> (space group *P6/mmm*). Np atoms (blue, large spheres) occupy the 1*a* Wyckoff position at 000 with point symmetry 6/*mmm*, whereas Ni atoms are located at the 2*c* (1/32/30,  $\bar{6}m2$ , red spheres) and 3*g* (1/201/2, *mmm*, green spheres) special positions. (b) Atom arrangements on the *z* = 0 and *z* = 1/2 planes (2 × 2 unit cells).

with localized 5*f* states from itinerant systems. Appreciable crystal field effects are therefore expected.

**B. Magnetic measurements**

The magnetic field ( $\mu_0 H$ ) dependence of the magnetization  $M(T, \mu_0 H)$  is shown in Fig. 3 for temperatures  $T$  equal to 2 and 5 K. The  $T$  dependence of  $M(T, \mu_0 H)$ , measured after field-cooling (FC) and zero-field-cooling (ZFC) conditions in a field  $\mu_0 H = 0.1$  T is shown in the inset. The observed magnetization curve is typical for a soft ferromagnet with vanishing coercive field and a Curie temperature  $T_C \simeq 16$  K, below which irreversibility effects associated to domain wall motions are observed. Below  $T_C$ , the magnetization saturates around  $\mu_0 H = 2$  T, reaching a value of  $\sim 2.2 \mu_B/\text{f.u.}$  at  $\mu_0 H = 7$  T. The temperature dependence of the inverse magnetic susceptibility  $H/M$ , measured up to 300 K in a field of 7 T, is shown in Fig. 4. Above  $\sim 40$  K, it can be fitted by the Curie-Weiss law with an effective paramagnetic moment  $\mu_{\text{eff}} = 3.69 \mu_B$  and a Curie-Weiss temperature  $\theta_{\text{CW}} = 14.7$  K.

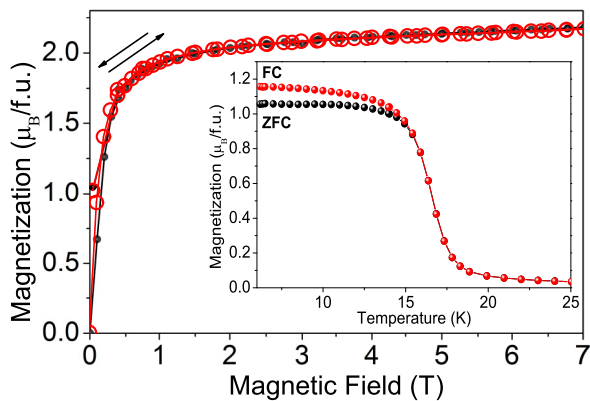


FIG. 3. (Color online) Magnetic field dependence of the magnetization measured on a polycrystalline sample of NpNi<sub>5</sub> at 2 K (black dots) and 5 K (red open circles). The inset shows the temperature dependence of the magnetization in a field  $\mu_0 H = 0.1$  T under field-cooled (FC) and zero-field-cooled (ZFC) conditions.

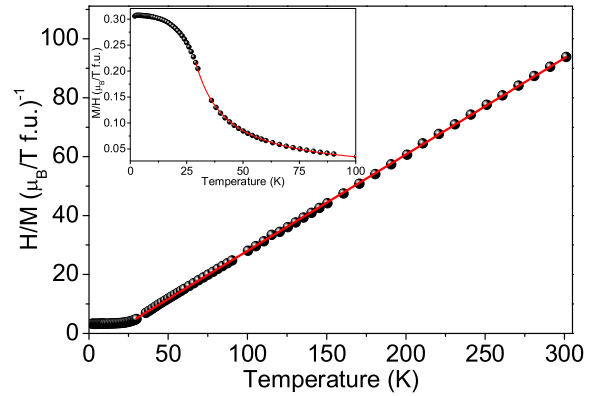


FIG. 4. (Color online) Temperature dependence of the NpNi<sub>5</sub> inverse magnetic susceptibility  $H/M$ , measured in a field  $\mu_0 H = 7$  T. The straight line is a fit to the Curie-Weiss law, giving an effective paramagnetic moment  $\mu_{\text{eff}} = 3.69 \mu_B$  and a Curie-Weiss temperature  $\theta = 14.7$  K. The temperature dependence of the susceptibility is shown in the inset.

The effective moment is very close to that of a Np<sup>4+</sup> free ion in intermediate coupling ( $3.8 \mu_B$ ), whereas it is much larger than for a trivalent ion ( $2.88 \mu_B$ ). However, the latter case cannot be excluded since the fact that the *ordered* moment on the Ni sites is very small (as determined in the next subsection) does not imply a negligible contribution to the *effective* moment. This was clearly shown in the case of NdNi<sub>5</sub> where the much larger than free ion value can be ascribed to the Ni contribution [24].

**C. Specific heat measurements**

Figure 5 shows the experimental data for both NpNi<sub>5</sub> and ThNi<sub>5</sub>. The anomaly observed at  $T_C$  for the former broadens and moves towards higher temperatures upon application of an external magnetic field, as expected for an anisotropic polycrystalline ferromagnetic sample.

The vibrational contribution has been estimated by subtracting a constant electronic term  $\gamma = 0.037 \text{ J K}^{-2} \text{ mol}^{-1}$  from the

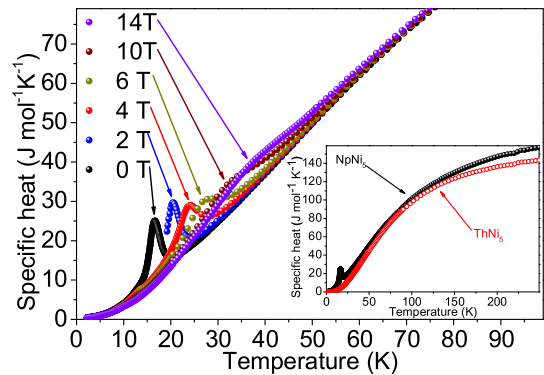


FIG. 5. (Color online) Temperature dependence of the specific heat measured for NpNi<sub>5</sub> in an external magnetic field with amplitude between 0 and 14 T. The specific heat curves measured from 2 to 300 K for (black circle) NpNi<sub>5</sub> and (red open circles) ThNi<sub>5</sub> are shown in the inset.

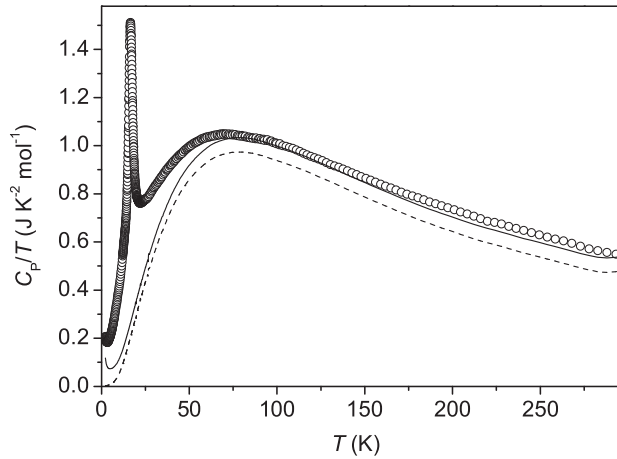


FIG. 6. Temperature dependence of the  $C_p/T$  ratio plotted as a function of  $T$ . The dashed line is the vibrational contribution estimated from the measurements performed on the isostructural compound  $\text{ThNi}_5$ . The full line is the sum of the vibrational contribution, a constant electronic term  $\gamma = 0.06 \text{ J K}^{-2} \text{ mol}^{-1}$ , and a nuclear Schottky contribution expressed as  $C_N/T^3$  with  $C_N = 0.625 \text{ J K/mol}$ .

$C_p/T$  measurements performed on  $\text{ThNi}_5$ , and is compared to the  $\text{NpNi}_5$  data in Fig. 6. The full background used in order to extract the magnetic contribution to the specific heat of  $\text{NpNi}_5$  is the sum of the vibrational contribution, a constant electronic term  $\gamma = 0.06 \text{ J K}^{-2} \text{ mol}^{-1}$ , and a nuclear Schottky contribution expressed as  $C_N/T^3$ , with  $C_N = 0.625 \text{ J K/mol}$  calculated from the Mössbauer splitting at 4 K. This has been subtracted by the  $C_p/T$  data of  $\text{NpNi}_5$  before integrating the result in order to obtain the temperature dependence of the magnetic entropy change (Fig. 7). Its behavior is qualitatively in line with that expected for  $\text{Np}^{3+}$ : At the jump around 16 K the entropy change is roughly equal to  $R\ln 2$ , indicating a doublet ground state. The full magnetic entropy for the lowest  $J$  manifold is recovered around room temperature.

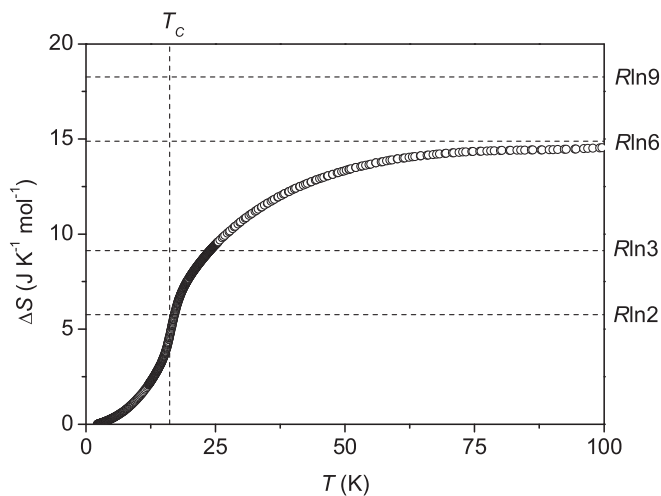


FIG. 7. Temperature dependence of the magnetic entropy change  $\Delta S$  extracted by numerically integrating the  $C_p/T$  data with the background subtracted.

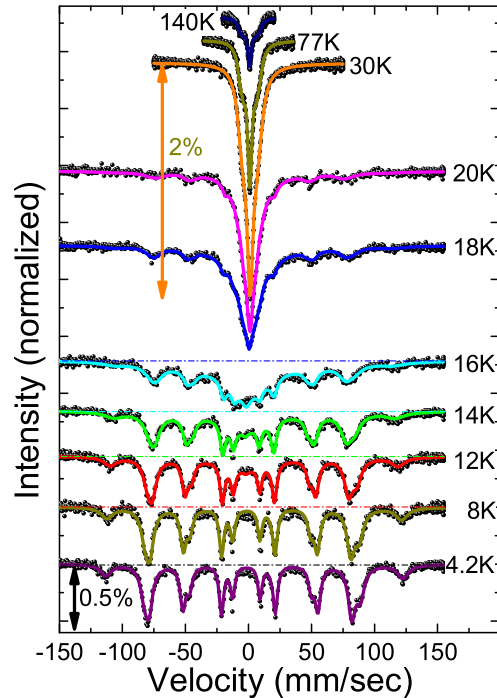


FIG. 8. (Color online) Temperature evolution of the Mössbauer spectra measured for  $\text{NpNi}_5$ . Dots are measured data, solid lines are the results of the fit to the model described in the text. Horizontal dashed lines indicate the baseline for each spectrum.

#### D. Mössbauer spectroscopy

$^{237}\text{Np}$  Mössbauer spectra recorded for  $\text{NpNi}_5$  at different temperatures, from 4.2 to 140 K, are shown in Fig. 8. A broadening of the central absorption line below 25 K seems to signal the occurrence of critical fluctuations, whereas a full magnetic splitting is observed below 14 K. Spectra calculated by solving the complete Hamiltonian for the hyperfine interactions, with a Lorentzian shape for the absorption lines, are shown by solid lines. The slight asymmetry of the magnetic split spectra is typical of systems dominated by magnetic interactions in the presence of weaker quadrupolar ones. A good fit is obtained by considering a single set of hyperfine parameters, which is consistent with the crystal structure of the compound. The main component of the electric field gradient ( $eq \equiv V_{zz}$ ) is taken collinear with the magnetization, and the asymmetry parameter ( $\eta$ ) is set to zero, because of the axial symmetry of the Np site.

The observed isomer shift is  $\delta_{IS} = -12.2 \text{ mm/s}$  with reference to  $\text{NpAl}_2$ , compatible with a  $5f^4$  trivalent state of Np in a metallic environment [25]. At 4.2 K the hyperfine field is  $B_{hf} = 437 \text{ T}$ , corresponding to an ordered magnetic moment at the Np site  $\mu_{\text{Np}} = 2.03(5) \mu_B$  ( $B_{hf}/\mu_{\text{Np}} = 215 \pm 5 \text{ T}/\mu_B$ ) [26], and the quadrupole coupling constant is  $e^2qQ \simeq -10.5 \text{ mm/s}$ . From the magnetization saturation value of  $2.2 \mu_B/\text{f.u.}$ , assuming as a crude approximation that the contribution of the conduction band is  $-10\%$  of the total magnetization, the average magnetic moment per Ni atom in  $\text{NpNi}_5$  is roughly estimated as  $\sim 0.08 \mu_B$ .

As shown in Fig. 9, the temperature dependence of the order parameter shows an abrupt step at  $T_C$  rather than a continuous

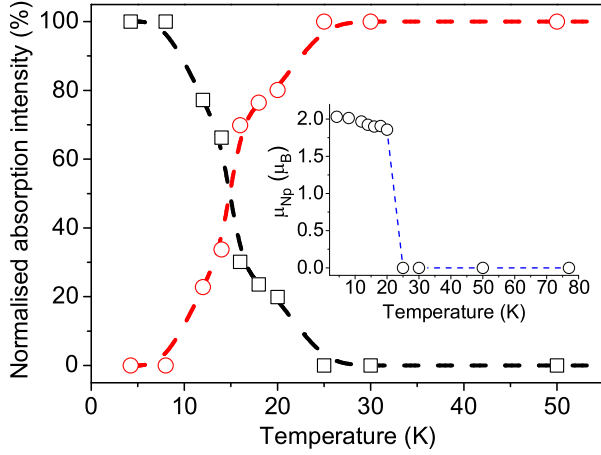


FIG. 9. (Color online) Temperature dependence of the relative integrated Mössbauer absorption intensities associated to the sextet (open black squares) and to the central absorption line (open red circles). The inset shows the temperature variation of the Np ordered moment, as deduced from the hyperfine field. Dashed lines are a guide to the eye.

decrease. At the same time, the Mössbauer absorption spectra show the persistence of both a broad central absorption peak below  $T_C$  and of a magnetic splitting above. These observations could indicate a first order nature of the phase transition. However, the absence of hysteresis in the magnetic and specific heat measurements, as well as their shape, do not support this conclusion. A different explanation involves crystal field effects as considered in the following sections.

### E. Crystal-field model

Given that the nature of  $5f$  electrons in NpNi<sub>5</sub> is expected to be essentially localized, we have attempted to model its properties by simple crystal-field (CF) calculations. The CF Hamiltonian appropriate for the  $D_{6h}$  symmetry of the Np sites is

$$H_{CF} = B_2^0 O_2^0 + B_4^0 O_4^0 + B_6^0 O_6^0 + B_6^6 O_6^6, \quad (1)$$

and reasonable values of the  $B_k^q$  parameters can be obtained by rescaling those determined for the isostructural PrNi<sub>5</sub> compound [27]. Table I gives the crystal-field splittings and the wave functions calculated for the lowest  $J$  multiplets of the  $5f^4$  (Np<sup>3+</sup>,  $J = 4$ ) configuration in the paramagnetic phase.

TABLE I. Crystal-field energy spectra in the paramagnetic phase calculated for Np<sup>3+</sup> in NpNi<sub>5</sub>. In the ordered phase the ground state becomes a singlet with composition  $0.927|+4\rangle - 0.375|-2\rangle$ .

$E$ (K)	Symmetry	Wave function
0	$\Gamma_5^{(1)}$	$0.917 \pm 4\rangle - 0.400 \mp 2\rangle$
21	$\Gamma_4$	$1/\sqrt{2} 3\rangle - 1/\sqrt{2} -3\rangle$
193	$\Gamma_1$	$ 0\rangle$
290	$\Gamma_6$	$ \pm 1\rangle$
487	$\Gamma_5^{(2)}$	$0.917 \pm 2\rangle - 0.400 \mp 4\rangle$
492	$\Gamma_3$	$1/\sqrt{2} 3\rangle + 1/\sqrt{2} -3\rangle$

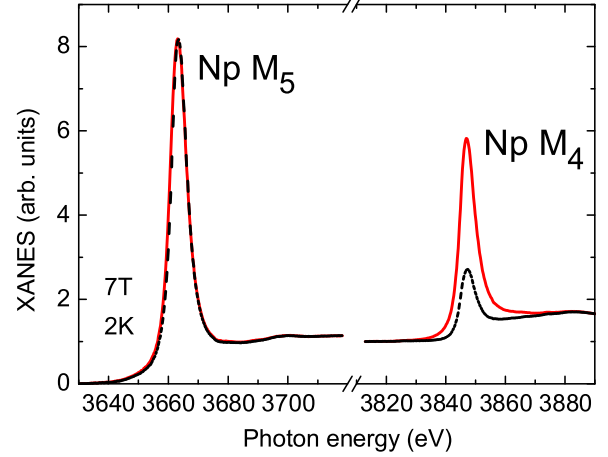


FIG. 10. (Color online) NpNi<sub>5</sub> x-ray absorption spectra recorded at the M<sub>5</sub> and M<sub>4</sub> Np edges for parallel ( $\mu^+(E)$ , dashed black line) and antiparallel ( $\mu^-(E)$ , solid red line) alignments of the photon helicity with respect to a 7 T external magnetic field applied along the beam direction (sample temperature 2 K). The spectra have been corrected for self-absorption effects and incomplete circular polarization of the incident beam.

### Adding the mean-field term

$$H_{MF} = \lambda g^2 \mu_B^2 [-J_z \langle J_z \rangle + \langle J_z \rangle^2 / 2] \quad (2)$$

with  $\lambda = 6.8 T/\mu_B$  triggers a second-order transition to a ferromagnetic state with the easy magnetization direction along the  $c$  axis, and reproduces exactly both the experimentally determined Curie temperature ( $T_C = 16$  K) and the ordered moment ( $2.03 \mu_B$ ).

### F. XMCD spectra

XMCD is associated with time-reversal symmetry breaking by a magnetic field and involves electric dipole or electric quadrupole transitions promoting an electron in a spin-orbit split core state to an empty valence state of the absorbing atom. The technique provides an element- and shell-specific probe for studying the electronic structure of a wide range of materials [28]. In this experiment, XMCD spectra have been measured at the  $M_{4,5}$  ( $3d_{3/2,5/2} \rightarrow 5f$ ) Np absorption edges.

The XAS spectra, measured with the sample kept at 2 K in a magnetic field of 7 T, are shown in Fig. 10 for both right- and left-circularly polarized x rays. The spectra have been corrected for self-absorption effects and for incomplete circular polarization rates of incident x-ray photons. The self-absorption corrections were done in the semi-infinite sample approximation, taking into account the chemical composition, the density, the background contributions (fluorescence of subshells and matrix, coherent and incoherent scattering), and the geometrical factors [29–31]. The Np edge-jump intensity ratio  $M_5/M_4$  has been normalized to 1.57, the value reported in the XCOM tables by Berger *et al.* in Ref. [32], which is close to the 1 : 2/3 statistical edge-jump ratio (defined as the ratio between the occupation numbers for the two spin-orbit-split core levels  $j = 3/2$  and  $5/2$ ).

The XMCD signal has been obtained as the difference of the corrected x-ray-absorption spectra,  $\Delta I_{M_{4,5}} = \mu^+(E) -$

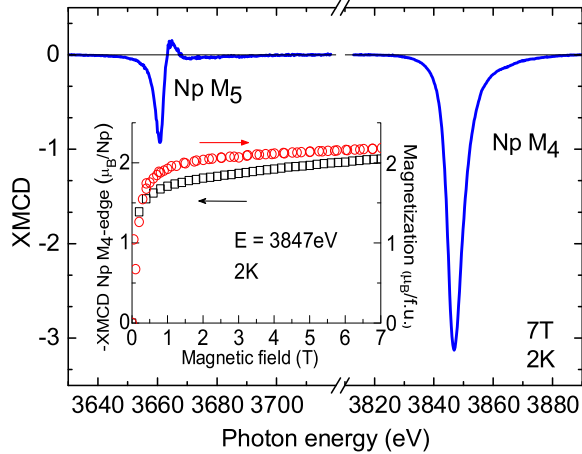


FIG. 11. (Color online) NpNi<sub>5</sub> XMCD spectra measured at the M<sub>5</sub> and M<sub>4</sub> Np edges in an applied field of 7 T at 2 K. The spectra have been corrected for self-absorption effects and for the incomplete circular polarization rate. Inset: (black squares) element-specific XMCD magnetization curve recorded at the maximum XMCD signal at the Np M<sub>4</sub> absorption edge ( $E = 3847$  eV) with the sample kept at 2 K, normalized to the ordered magnetic moment obtained by Mössbauer spectroscopy; (red circles) SQUID magnetization curve measured at 2 K.

$\mu^-(E)$ , whereas the white line intensities  $I_{M_{4,5}}$  were obtained after a subtraction of a step function convoluted by a Voigt line shape, in order to remove contributions due to transitions into the continuum. The results are shown in Fig. 11, together with the field dependence of the dichroic signal at the M<sub>4</sub> edge, normalized at 7 T to the value of the Np ordered magnetic moment deduced from Mössbauer spectroscopy. This provides a Np-specific magnetization curve, which is compared with the magnetization measured by SQUID at 2 K. The difference between the two data sets provides the conduction electrons and Ni sublattice contributions to the total magnetization.

The orbital and spin contributions to the total magnetic moment carried by the Np atoms can be separately determined by appropriate sum rules [33,34]. In particular, the ground state expectation value of the orbital moment is obtained from the total dichroic signal,  $\Delta I_{M_5} + \Delta I_{M_4}$ , as [35]

$$\langle L_z \rangle = \frac{n_h}{I_{M_5} + I_{M_4}} (\Delta I_{M_5} + \Delta I_{M_4}) \quad (3)$$

where  $I_{M_{4,5}}$  is the integrated intensity of the isotropic x-ray absorption spectrum at the Np M<sub>4,5</sub> edges, and  $n_h$  is the number of holes in the 5f shell. The spin polarization  $\langle S_z \rangle$  is instead obtained from a second sum rule, stating that [36]

$$\langle S_z \rangle + 3\langle T_z \rangle = \frac{n_h}{2(I_{M_5} + I_{M_4})} \left( \Delta I_{M_5} - \frac{3}{2} \Delta I_{M_4} \right), \quad (4)$$

where the so-called magnetic dipole term  $T_z$  is the component along the quantization axis of an operator associated to charge and magnetic anisotropy [37] and correlating spin  $\vec{s}_i$  and position  $\vec{r}_i$  of individual electrons,  $\vec{T} = \sum_i [\vec{s}_i - 3(\vec{r}_i \cdot \vec{s}_i)/r_i^2]$ . Furthermore, the expectation value of the angular part of the valence states spin-orbit operator,  $\langle \psi | \vec{\ell} \cdot \vec{s} | \psi \rangle$ , can be obtained

TABLE II. Comparison between moments deduced from combining XMCD and Mössbauer results and corresponding values calculated with the mean-field model for Np<sup>3+</sup> ions, as described in the text.

	Obs.	Calc.
$\mu_{\text{Np}} (\mu_B)$	2.03	2.03
$\langle L_z \rangle$	-3.91	-4.27
$\langle S_z \rangle + 3\langle T_z \rangle$	2.26	1.75
$\langle \vec{\ell} \cdot \vec{s} \rangle$	-5.55	-6.26

from the XAS branching ratio,  $B = I_{M_5}/(I_{M_5} + I_{M_4})$ , as [38]

$$\frac{2\langle \vec{\ell} \cdot \vec{s} \rangle}{3n_h} - \Delta = -\frac{5}{2} \left( B - \frac{3}{5} \right), \quad (5)$$

where  $\Delta$  is a quantity dependent from the electronic configuration [34] (for Np<sup>3+</sup>,  $\Delta = -0.005$ ) and the experiment provides an isotropic branching ratio  $B = 0.746(5)$ . Assuming  $n_h = 10$ , from Eq. (5) one obtains  $\langle \vec{\ell} \cdot \vec{s} \rangle = -5.55$ , a value close to the one (-6.25) calculated in the intermediate coupling approximation for Np<sup>3+</sup> free ions [33]. Moreover, as  $\langle \psi | \vec{\ell} \cdot \vec{s} | \psi \rangle = 3n_{7/2}^{5f}/2 - 2n_{5/2}^{5f}$ , one obtains for the occupation numbers of the  $j = 5/2$  and  $j = 7/2$  5f subshells  $n_{5/2}^{5f} = 3.3$  and  $n_{7/2}^{5f} = 0.7$  ( $n_{5/2}^{5f} + n_{7/2}^{5f} = 4$ ).

Inserting in Eq. (3) the experimental values  $\Delta I_{M_5} = -4.3037$ ,  $\Delta I_{M_4} = -27.1271$ , and  $I_{M_5} + I_{M_4} = 80.4663$ , one obtains  $\langle L_z \rangle = -3.91$ , and therefore  $\mu_L = 3.91 \mu_B$ . The total Np moment, as given by the Mössbauer hyperfine field, is  $\mu_{\text{Np}} = \mu_L + \mu_S = 2.03 \mu_B$ , and one obtains  $\mu_S = -1.88 \mu_B$  and  $\langle S_z \rangle = 0.94$ . Table II lists some parameters and observables obtained from XMCD data assuming a trivalent oxidation state for neptunium, compared with the same quantities calculated for the ground state in the ordered phase by the mean-field model outlined in the previous subsection.

From Eqs. (3) and (4) one obtains  $\langle S_z \rangle + 3\langle T_z \rangle = 2.26$ . This corresponds to  $\langle T_z \rangle = 0.44$  and to a ratio  $3\langle T_z \rangle/\langle S_z \rangle = +1.43$ , which differ by about 5% from the value of +1.36 obtained by similar experiments in Np<sub>2</sub>Co<sub>17</sub> [25], which is also a localized system, but is about 70% larger than the value (0.83) found for the itinerant ferromagnet NpOs<sub>2</sub> [39].

#### IV. FIRST-PRINCIPLE CALCULATIONS

To examine theoretically the electronic structure of NpNi<sub>5</sub> and to make a comparison with experimental data, we performed spin-polarized local spin density approximation (LSDA) as well as LSDA plus Hubbard U (LSDA+U) calculations, using the experimental lattice parameters listed above. All calculations are performed making use of the in-house implementation [40,41] of the full-potential linearized augmented plane wave (FP-LAPW) method. This FP-LAPW version includes all relativistic effects: scalar-relativistic and spin-orbit coupling (SOC). The radii of the atomic muffin-tin (MT) spheres are set to 2.8 a.u. (Np) and 2.1 a.u. (Ni). The basis set size is characterized by the parameter  $R_{\text{Np}} \times K_{\text{max}} = 8.4$ , and the Brillouin zone is sampled with 765  $k$  points.

TABLE III. Spin ( $\mu_S$ ), orbital ( $\mu_L$ ), and total ( $\mu = \mu_S + \mu_L$ ) magnetic moments in the “muffin-tin” spheres around Np and Ni atoms (in  $\mu_B$  units), together with total values (including interstitial contributions) per formula unit (f.u.) of  $\mu_S$ ,  $\mu_L$ , and  $\mu$ .

Atom	Site	LSDA(+SOC)			AMF-LSDA+U			$\mu_{\text{exp}}$
		$\mu_S$	$\mu_L$	$\mu$	$\mu_S$	$\mu_L$	$\mu$	
Np	1a	-2.89	2.92	-0.03	-1.63	3.93	2.30	2.03
Ni <sub>1</sub>	2c	0.20	-0.04	0.20	0.11	-0.04	0.07	0.08 <sup>a</sup>
Ni <sub>2</sub>	3g	0.23	0.00	0.23	0.19	0.00	0.19	0.08 <sup>a</sup>
Total		-2.08	2.84	0.76	-0.96	3.81	2.85	2.2 <sup>b</sup>

<sup>a</sup>Average obtained by dividing the Ni sublattice moment by the number of sites.

<sup>b</sup>From magnetization data.

First, we apply the conventional spin-polarized LSDA, assuming antiparallel coupling between Ni-3d and Np-5f spin moments [42]. Table III reports the calculated spin ( $\mu_S$ ), orbital ( $\mu_L$ ), and total ( $\mu = \mu_S + \mu_L$ ) magnetic moments in the “muffin-tin” spheres around Np and Ni atoms (in  $\mu_B$  units), together with the total values (including contributions from the interstitial region) per formula unit (f.u.) of  $\mu_S$ ,  $\mu_L$ , and  $\mu$ . It is seen that LSDA yields a substantially smaller value of the magnetization/f.u. ( $0.76 \mu_B$ ) than experimentally observed ( $2.2 \mu_B$ ).

Next, we apply LSDA+U calculations, making use of relativistic (including SOC) “around-mean-field” (AMF)-LSDA+U, Ref. [40]. The Coulomb interaction in the Np 5f shell is parameterized by Slater integrals  $F_0 = 3.00$  eV,  $F_2 = 7.43$  eV,  $F_4 = 4.83$  eV, and  $F_6 = 3.53$  eV, as given in Ref. [43]. They correspond to commonly accepted values  $U = 3$  eV and  $J = 0.6$  eV for the Coulomb and exchange interactions parameters, respectively.

The total electron-energy density of states (DOS) calculated for  $U = 3$  eV is shown in Fig. 12, together with spin-resolved  $d$ -orbital projected DOS for Ni atoms at the occupied lattice sites and  $f$ -orbital projected DOS for Np atom. The Ni- $d^\uparrow$  band is practically full, whereas the Ni- $d^\downarrow$  band is partially occupied. The DOS peak in the vicinity of the Fermi level ( $E_F$ ) has mostly Ni- $d^\downarrow$  character.

The occupied part of Np- $f$  manifold is mostly located in the energy range from 1 eV to 3 eV below  $E_F$ , and the 5f electrons are therefore essentially localized. Their contribution to the spin ( $\mu_S^{5f} = -2\langle S_z^{5f} \rangle \mu_B / \hbar$ ) and orbital ( $\mu_L^{5f} = -\langle L_z^{5f} \rangle \mu_B / \hbar$ ) magnetic moments as well as the magnetic dipole  $\mu_{md}^{5f} = -6\langle T_z \rangle \mu_B / \hbar$  contribution are given in Table IV, together with the calculated occupation numbers ( $n^{5f}$ ,  $n_{5/2}^{5f}$  and  $n_{7/2}^{5f}$ ), the Np  $M_{4,5}$ -edges branching ratio  $B$ , and the valence spin-orbit interaction ( $\langle \vec{\ell} \cdot \vec{s} \rangle$ ) [from Eq. (5)]. These quantities can be directly compared with those deduced from the shell-specific XMCD spectra measured at the Np  $M_{4,5}$  absorption edges.

The 5f occupation number is about 3.8, closer to the Np<sup>3+</sup> case. Using the values from Table IV one obtains  $\langle L_z \rangle = -3.98$ ,  $\langle S_z \rangle + 3\langle T_z \rangle = 2.22$ ,  $\langle \vec{\ell} \cdot \vec{s} \rangle = -5.68$ , and the branching ratio  $B = 0.75$ , together with the  $f$ -shell magnetization of  $2.3 \mu_B$ . All of these numbers are in reasonable

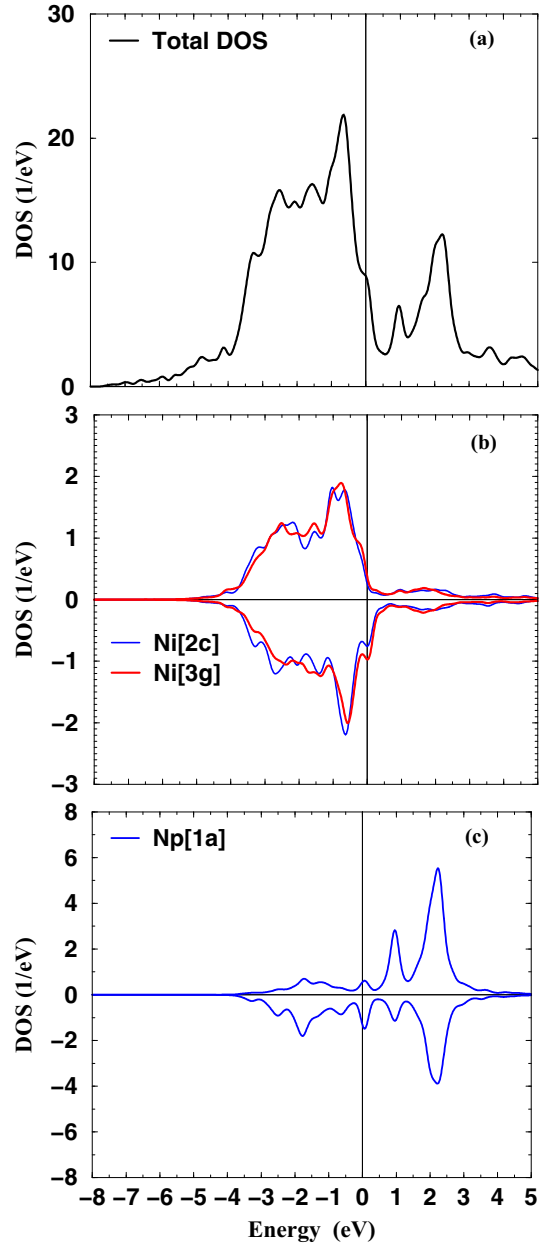


FIG. 12. (Color online) (a) The total electron-energy density of states (DOS) per formula unit for NpNi<sub>5</sub> calculated with relativistic LSDA+U ( $U = 3$  eV); (b) the  $d$ -orbital projected DOS for Ni atoms at [2c], and [3g] special positions of the  $P6/mmm$  space group; (c) the  $f$ -orbital projected DOS for Np atoms at [1a] position.

TABLE IV. 5f-states occupations  $n^{5f}$ ,  $n_{5/2}^{5f}$ , and  $n_{7/2}^{5f}$ , branching ratio  $B$ , and 5f-electron contribution to the valence spin-orbit interaction per hole  $w^{110}/n_h$ , and the spin, orbital, and magnetic-dipole moments ( $\mu_S^{5f}$ ,  $\mu_L^{5f}$ , and  $\mu_{md}^{5f}$ ) in Bohr magneton ( $\mu_B$ ) units.

Atom [Site]	$n^{5f}$	$n_{5/2}^{5f}$	$n_{7/2}^{5f}$	$B$	$\langle \vec{\ell} \cdot \vec{s} \rangle$	$\mu_S^{5f}$	$\mu_L^{5f}$	$\mu_{md}^{5f}$
LSDA(+SOC)								
Np[1a]	3.73	2.59	1.15	0.69	-3.45	-2.74	2.90	-0.37
AMF-LSDA+U								
Np[1a]	3.77	3.24	0.53	0.75	-5.68	-1.63	3.98	-2.81

agreement with the experimental data listed in Table II for  $\text{Np}^{3+}$ .

## V. DISCUSSION

A comparison between XMCD results and first-principle calculations supports the assumption that the Np ions in  $\text{NpNi}_5$  are trivalent. The Np ordered magnetic moment at 4 K, about 20% smaller than the  $\text{Np}^{3+}$  free ion values ( $\mu = 2.57 \mu_B$ ), suggests a rather localized nature of the  $5f$  electrons. This is supported by the results of first-principle calculations that locate the Np- $f$  manifold in the energy range from 1 eV to 3 eV below the Fermi level. The moment reduction can be attributed to the crystal-field potential. The  $f$ -electron behavior is therefore similar to the rare-earth analogs. However, whereas for the latter the Ni  $d$  band is completely filled and magnetically inert, here one component of the spin-polarized Ni  $d$  band is only partially filled. This is reflected in the value of the effective paramagnetic moment, which is higher than the free ion value for  $\text{Np}^{3+}$ .

The specific heat data suggest that the ground state is a doublet, and a simple mean-field calculation is sufficient to obtain a good agreement with the values observed for the ordered moment and its spin and angular components. In the analog  $\text{RNi}_5$  series, the sign of  $B_2^0$  usually determines the preferred orientation of the magnetic moment, which is along the  $c$  axis for negative  $B_2^0$  (e.g., for Er, Tm), and in the basal plane if  $B_2^0 > 0$  (e.g., for Nd, Tb, Dy, Ho) [44] although, as observed for other rare-earth intermetallic systems [45,46], high-order terms in the crystal field potential are expected to play an important role in determining the magnetic anisotropy. For  $\text{Np}^{3+}$ , the Stevens factor  $\alpha_J$  is positive ( $\alpha_J = 9.13 \times 10^{-3}$  in intermediate coupling approximation [47]), whereas the lattice electric field gradient  $V_{zz}^{\text{latt}}$  should be positive, as observed for the isostructural  $\text{GdNi}_5$  compound [48]. Thus  $B_2^0 \propto -\alpha_J V_{zz}^{\text{latt}}$  is negative in  $\text{NpNi}_5$ , and the Np magnetic moments point along the  $c$  axis, and the ground state is a  $\Gamma_5$  doublet (note that in the ordered state of  $\text{NpNi}_5$  the  $z$  axis of the electric field gradient  $V_{zz}$  is given by the direction of the ordered magnetic moment).

The electronic  $5f$  contribution to the quadrupole interaction is proportional to  $\langle 3J_z^2 - J(J+1) \rangle \simeq 23$ . For the  $\text{Np}^{3+}$  free ion,  $\langle 3J_z^2 - J(J+1) \rangle = 28$ , and the quadrupole interaction due to the  $5f$  electrons amounts to  $-27.3$  mm/s [49]. It follows that  $eV_{zz}^{5f} Q(1-R)$  is negative and equal to  $-22.45$  mm/s. In addition to this electronic contribution, the quadrupole interaction acting on the Np nuclei contains also a contribution from the lattice and the conduction electrons,  $eV_{zz}^{\text{latt}} Q(1-\gamma_\infty)$ , where  $\gamma_\infty$  is the Sternheimer factor. A rough estimate of this contribution can be provided by the quadrupole interaction measured for  $\text{GdNi}_5$  [48], where the  $f$  contribution to  $V_{zz}$  vanishes, as  $\text{Gd}^{3+}$  are  $S$ -state ions. From  $eV_{zz} Q = 4.68$  mm/s in  $\text{GdNi}_5$  and using the quadrupole moment  $Q = 1.3 \times 10^{-24}$  cm<sup>2</sup> for <sup>155</sup>Gd nuclei [50], it follows that  $V_{zz}^{\text{latt}}(1-\gamma_\infty) = 10.4 \times 10^{-7}$  V/cm<sup>2</sup>. Assuming that  $V_{zz}^{\text{latt}}$  for both  $\text{NpNi}_5$  and  $\text{GdNi}_5$  are identical, and taking the values of  $\gamma_\infty$  of  $-92$  and  $-130$  for Gd and Np, respectively [51,52], one obtains for  $\text{NpNi}_5$   $V_{zz}^{\text{latt}}(1-\gamma_\infty) = 14.6 \times 10^{17}$  V/cm<sup>2</sup> and  $eV_{zz}^{\text{latt}}(1-\gamma_\infty)Q = 30.2$  mm/s, using the value of  $4.1 \times 10^{-24}$  cm<sup>2</sup>

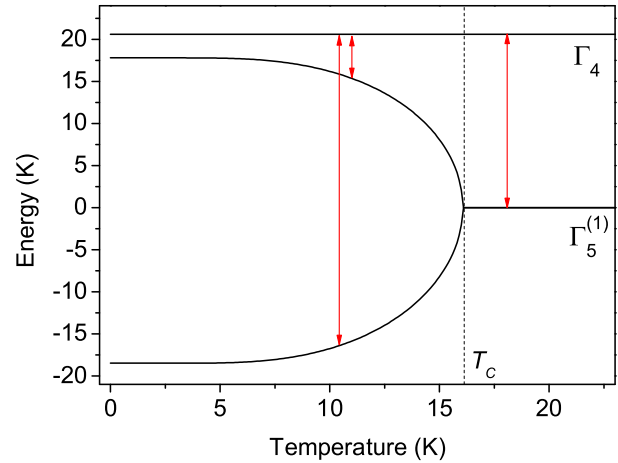


FIG. 13. (Color online) Splitting of the low-energy crystal field levels by the molecular field in the ordered phase. The arrows indicate the allowed spin relaxation  $\Delta J_z = \pm 1$  pathways between the levels of the ground quasitriplet.

for the quadrupole moment of the <sup>237</sup>Np nuclei ground state [26] ( $1 \text{ mm/s} = 19.86 \times 10^{-8} \text{ eV}$ ). As the principal axis of the lattice contribution to the electric field gradient is also parallel to the crystallographic  $c$  axis, the estimated total quadrupole interaction in the low-temperature ordered state is  $eV_{zz} Q = 7.8$  mm/s, relatively close to the experimental value of  $-10.5$  mm/s. The difference between observed and calculated values can be attributed to the approximations made above, namely a fully localized  $5f$  electronic configuration and equal lattice contributions for  $\text{NpNi}_5$  and  $\text{GdNi}_5$ .

As shown in Table I, in the paramagnetic phase the low-energy crystal field level scheme is characterized by a doublet ground state with an excited singlet at 21 K. Direct spin relaxation is highly suppressed within the  $\Gamma_5$  doublet but allowed via the excited singlet [53,54]. As long as the relaxation rate is slow, we observe the coexistence of a magnetic split pattern and of a somewhat broadened quadrupole spectrum, for example at 20 K (Fig. 8). With increasing temperature, the singlet becomes more and more populated, the spin-relaxation rate speeds up, the magnetic split pattern collapses, and the quadrupolar spectrum becomes less and less broad, until the limit of fast relaxation is reached. Below  $T_C$ , the doublet is split by the molecular field, as depicted in Fig. 13. However, a quadrupole split spectrum is still observed, together with the full-split pattern originating from the ground state, as long as the singlet is thermally populated. When the temperature is low enough, only the ground state is populated, the relaxation slows down, and the hyperfine field is almost temperature independent.

## VI. CONCLUSIONS

The low-temperature physical behavior of  $\text{NpNi}_5$  has been investigated by magnetization, Mössbauer spectroscopy, specific heat, and x-ray magnetic circular dichroism measurements. The compound crystallizes in the  $\text{CaCu}_5$ -type hexagonal structure and, at  $T_C \sim 16$  K, undergoes a transition to a ferromagnetic state. The results suggest a trivalent



oxidation state for neptunium ( $5f^4$  electronic configuration), and an ordered moment at the Np site of  $\sim 2 \mu_B$  is obtained by Mössbauer spectroscopy. The Ni up-spin  $3d$  band is almost filled whereas the down-spin one is only partially occupied, resulting in a magnetic moment at the Ni sites of about  $0.08 \mu_B$ . The peculiar temperature dependence of the Mössbauer spectra is explained by the presence of two separate relaxation phenomena within the sublevels of the ground quartet.

Combining XMCD and Mössbauer spectroscopy results, we obtain the spin and orbital contributions to the Np magnetic moment ( $\mu_S = -1.88 \mu_B$  and  $\mu_L = 3.91 \mu_B$ ). The ratio between the expectation value of the magnetic dipole operator and the spin magnetic moment is positive and large, as predicted for localized  $5f$  electrons. The expectation value of the angular part of the spin-orbit interaction operator is in good agreement with the value calculated in intermediate coupling approximation for Np ions. The temperature dependence of the specific heat shows a narrow anomaly at  $T_C$ , which broadens and shifts towards higher temperatures when an external magnetic field is applied. The vibrational contribution to the specific heat has been estimated from the curve measured for

ThNi<sub>5</sub>. This allowed us to determine the magnetic entropy change that gives information on the electronic energy level distribution. Although the  $5f$ -electron narrow band is well below the Fermi energy, the overall magnetic behavior is essentially different from the localized rare earth case, mostly due to the contributions of the nickel sublattice.

#### ACKNOWLEDGMENTS

We thank D. Bouëxière, G. Pagliosa, and P. Amador, for their technical support. The high-purity neptunium metal required for the fabrication of the sample was made available through a loan agreement between Lawrence Livermore National Laboratory and ITU, in the frame of a collaboration involving LLNL, Los Alamos National Laboratory, and the U.S. Department of Energy. A.H. acknowledges the European Commission for support in the frame of the Training and Mobility of Researchers programme. The support from Czech Republic Grant No. GACR P204/10/0330 is acknowledged.

- 
- [1] M. Akabori, R. G. Haire, J. K. Gibson, Y. Okamoto, and T. Ogawa, *J. Alloys & Compnds.* **257**, 268 (1997).
- [2] W. H. Zachariasen, *J. Inorg. Nucl. Chem.* **35**, 3487 (1973).
- [3] H. Hill, *Plutonium 1970 and Other Actinides*, edited by W. N. Miner (AIME, New York, 1971), p. 2.
- [4] J. H. N. van Vucht, F. A. Kuijpers, and H. C. A. M. Bruning, *Philips Res. Rep.* **25**, 133 (1970).
- [5] F. A. Kuijpers, *Philips Res. Rep. Suppl.* **28**, 1 (1973).
- [6] T. Takeshita, K. A. Gschneider, Jr., D. K. Thome, and O. D. McMasters, *Phys. Rev. B* **21**, 5636 (1980).
- [7] A. Szajek, M. Jurczyk, M. Nowak, and M. Makowiecka, *Phys. Status Solidi (a)* **196**, 252 (2003).
- [8] Y. Yu, H. Han, Y. Zhao, W. Xue, and T. Gao, *Solid State Commun.* **148**, 1 (2008).
- [9] E. A. Goremychkin, E. Mühle, B. Lippold, O. D. Chistyakov, and E. M. Savitskii, *Phys. Status Solidi (b)* **127**, 371 (1985).
- [10] V. M. T. S. Barthem, D. Gignoux, A. Nait-Saada, D. Schmitt, and G. Creuzet, *Phys. Rev. B* **37**, 1733 (1988).
- [11] M. Reiffers, Y. G. Naidyuk, A. G. M. Jansen, P. Wyder, I. K. Yanson, D. Gignoux, and D. P. Schmitt, *Phys. Rev. Lett.* **62**, 1560 (1989).
- [12] P. C. M. Gubbens, A. M. van der Kraan, and K. H. J. Buschow, *Phys. Rev. B* **39**, 12548 (1989).
- [13] A. Amato, W. Bühner, A. Grayevsky, F. N. Gyax, A. Furrer, N. Kaplan, and A. Schenck, *Solid State Commun.* **82**, 767 (1992).
- [14] P. Novák and J. Kuriplach, *Phys. Rev. B* **50**, 2085 (1994).
- [15] P. Svoboda, J. Vejpravová, N.-T. Kim-Ngan, and F. Kaysel, *J. Magn. Magn. Mater.* **272–276**, 595 (2004).
- [16] K. H. J. Buschow, *Rep. Prog. Phys.* **40**, 1179 (1977).
- [17] D. Gignoux, F. Givord, and A. Del Moral, *Solid State Commun.* **19**, 891 (1976).
- [18] H. Folle, M. Kubota, C. Buchal, R. Mueller, and F. Pobell, *Z. Phys. B* **41**, 223 (1981).
- [19] K. Andres and S. Darack, *Physica B+C* **86–88**, 1071 (1977).
- [20] A. G. Kuchin, A. M. Gurevich, V. M. Dmitriev, A. V. Terekhov, T. V. Chagovets, and A. S. Ermolenko, *J. Alloys & Compnds.* **368**, 75 (2004).
- [21] A. G. Kuchin, A. S. Ermolenko, Y. A. Kulikov, V. I. Khrabrov, E. V. Rosenfeld, G. M. Makarova, T. P. Lapina, and Y. V. Belozero, *J. Magn. Magn. Mater.* **303**, 119 (2006).
- [22] P. Santini, S. Carretta, N. Magnani, G. Amoretti, and R. Caciuffo, *Phys. Rev. Lett.* **97**, 207203 (2006).
- [23] N. Magnani, S. Carretta, R. Caciuffo, P. Santini, G. Amoretti, A. Hiess, J. Rebizant, and G. H. Lander, *Phys. Rev. B* **78**, 104425 (2008).
- [24] V. M. T. S. Barthem, D. Gignoux, A. Nait-Saada, D. Schmitt, and A. Y. Takeuchi, *J. Magn. Magn. Mater.* **80**, 142 (1989).
- [25] I. Halevy, A. Hen, I. Orion, E. Colineau, R. Eloidri, J.-C. Griveau, P. Gaczyński, F. Wilhelm, A. Rogalev, J.-P. Sanchez, M. L. Winterrose, N. Magnani, A. B. Shick, and R. Caciuffo, *Phys. Rev. B* **85**, 014434 (2012).
- [26] B. D. Dunlap and G. M. Kalvius, in *Handbook on the Physics and Chemistry of the Actinides*, edited by A. J. Freeman and G. H. Lander (North-Holland, Amsterdam, 1985), Vol. 2, p. 329.
- [27] K. Andres, S. Darack, and H. R. Ott, *Phys. Rev. B* **19**, 5475 (1979).
- [28] G. van der Laan, *J. Phys.: Conf. Ser.* **430**, 012127 (2013).
- [29] J. Goulon, C. Goulon-Ginet, R. Cortes, and J. M. Dubois, *J. Phys. (Paris)* **43**, 539 (1982).
- [30] L. Tröger, D. Arvanitis, K. Baberschke, H. Michaelis, U. Grimm, and E. Zschech, *Phys. Rev. B* **46**, 3283 (1992).
- [31] P. Pfalzer, J.-P. Urbach, M. Klemm, S. Horn, M. L. denBoer, A. I. Frenkel, and J. P. Kirkland, *Phys. Rev. B* **60**, 9335 (1999).
- [32] M. J. Berger, J. H. Hubbell, S. M. Seltzer, J. Chang, J. S. Coursey, R. Sukumar, D. S. Zucker, and K. Olsen, <http://www.nist.gov/pml/data/xcom>.
- [33] G. van der Laan and B. T. Thole, *Phys. Rev. B* **53**, 14458 (1996).

- [34] G. van der Laan, K. T. Moore, J. G. Tobin, B. W. Chung, M. A. Wall, and A. J. Schwartz, *Phys. Rev. Lett.* **93**, 097401 (2004).
- [35] B. T. Thole, P. Carra, F. Sette, and G. van der Laan, *Phys. Rev. Lett.* **68**, 1943 (1992).
- [36] P. Carra, B. T. Thole, M. Altarelli, and X. Wang, *Phys. Rev. Lett.* **70**, 694 (1993).
- [37] S. P. Collins, D. Laundry, C. C. Tang, and G. van der Laan, *J. Phys.: Condens. Matter* **7**, 9325 (1995).
- [38] B. T. Thole and G. van der Laan, *Phys. Rev. A* **38**, 1943 (1988).
- [39] F. Wilhelm, R. Eloirdi, J. Ruzs, R. Springell, E. Colineau, J.-C. Griveau, P. M. Oppeneer, R. Caciuffo, A. Rogalev, and G. H. Lander, *Phys. Rev. B* **88**, 024424 (2013).
- [40] A. B. Shick, D. L. Novikov, and A. J. Freeman, *Phys. Rev. B* **56**, R14259(R) (1997).
- [41] A. B. Shick and W. E. Pickett, *Phys. Rev. Lett.* **86**, 300 (2001).
- [42] M. Brooks, O. Eriksson, and B. Johansson, *J. Phys.: Condens. Matter* **1**, 5861 (1989).
- [43] K. T. Moore and G. van der Laan, *Rev. Mod. Phys.* **81**, 235 (2009).
- [44] D. Gignoux and D. Schmitt, in *Handbook of Magnetic Materials*, edited by K. H. W. Buschow (North-Holland, Amsterdam, 1997), Vol. 10, p. 239.
- [45] O. Moze, R. M. Ibberson, R. Caciuffo, and K. H. J. Buschow, *J. Less-Common Met.* **166**, 329 (1990).
- [46] R. Caciuffo, G. Amoretti, K. H. J. Buschow, O. Moze, A. P. Murani, and B. Paci, *J. Phys.: Condens. Matter* **7**, 7981 (1995).
- [47] G. Amoretti, *J. Phys. (Paris)* **45**, 1067 (1984).
- [48] F. J. van Steenwijk, H. T. Lefever, R. C. Thiel, and K. H. J. Buschow, *Physica B+C* **92**, 52 (1977).
- [49] J.-P. Sanchez, P. Burlet, S. Quezel, D. Bonnissseau, J. Rossat-Mignod, J.-C. Spirlet, and O. Vogt, *Solid State Commun.* **67**, 999 (1988).
- [50] Y. Tanaka, D. B. Laubacher, R. M. Steffen, E. B. Shera, H. D. Wohlfahrt, and M. V. Hoehn, *Phys. Lett. B* **108**, 8 (1992).
- [51] W. A. Barton and J. D. Cashion, *J. Phys. C* **12**, 2897 (1979).
- [52] T. Thevenin and A. Cousson, *J. Solid State Chem.* **67**, 254 (1987).
- [53] G. M. Kalvius, W. Potzel, J. Moser, F. J. Litterst, L. Asch, J. Zänkert, U. Potzel, A. Kratzer, M. Wunsch, J. Gal, S. Fredo, D. Dayan, M. P. Dariel, M. Boge, J. Chappert, J. C. Spirlet, U. Benedict, and B. D. Dunlap, *Physica B+C* **130**, 393 (1985).
- [54] J. Gal, H. Pinto, S. Fredo, M. Melamud, H. Shaked, R. Caciuffo, F. J. Litterst, L. Asch, W. Potzel, and G. Kalvius, *J. Magn. Magn. Mater.* **50**, L123 (1985).